Dynamics of a 2D Elastic Machinery Casing, with a Central Hole, Subject to an In-Plane Deflection-Dependent Rotating Load

F. M. A. El-Saeidy[1]

Abstract: In rotating radial ball bearings supported on elastic casings with the bearing outer ring lightly fitted into the housing, the force due to the ball elastic contact is indeed a rotating load rolling over the housing. For accurate estimation of the dynamic deformations of the casing annulus (hole), which in turn affect the bearing tolerances and hence the magnitudes of the generated forces, effect of the load rotation (motion) should be considered. Considering the integral casing and the outer ring to be a plate, an isoparametric plane stress finite-element (FE) based analytical procedure is presented for the dynamic analysis of the housing as affected by the load vector rotation. The Hertz equation for elastic contact is used to model the nonlinear elastic coupling between the external moving load and the vibrations of the housing. The equations of motion are obtained using Lagrange's equations and decoupled using the normal coordinates representation and solved using a special numerical integration scheme. The computations are carried out using the FE program 'DAMRO 1' and the results are discussed using time domain, motions in the state plane, Poincare' return map, and FFT. The results show that the overall amplitudes of the deformation vector around the annulus circumference and hence amplitudes of the dynamic load vary between maximum in the direction of the casing rigid support and minimum in the orthogonal direction. These regular variations can initiate/accelerate fatigue in the elastic components of the system. The vibrations measured at the casing outer surface show that the dominant peak in the horizontal direction and the one in the vertical direction do not coincide. And this recommends using one vibration measuring probe in the horizontal direction and another probe in the vertical direction, to capture all the important vibrations.

keyword: Machinery casing, in-plane moving load, nonlinear interaction, plate finite-elements.

1 Introduction

Flat plates are widely used in practice, ranging from, for example, a single plate supporting a shaft bearing to a collection of plates constitute a gear box casing, etc. The applied loads on the elastic member can be pure in-plane, or lateral, or a combination of both. and they can be stationary or moving. As a result, the plate will vibrate in its plane or laterally, or both. The study of flat plates under lateral moving loads had received much work using, for example, integral transformations methods [Fryba (1972)] and approximate techniques such as finite-elements method (FEM) [Taheri and Ting (1988)]. To the author's knowledge, the first study of a flat plate subject to an in-plane moving load was presented by El-Saeidy (1999) where the external moving force was of constant magnitude (for more information on the recent works on structures under moving loads, see for example, the reviewed papers in [El-Saeidy (2000)]. And the published studies are limited to in-plane stationary concentrated/distributed forces, to primarily determine the plate buckling loads and/or the related vibrations. For example, see Leissa and Ayoup (1988), Laura and Gutherrez (1998), and Yang (1986). Taha and Crookail (1977) used an existing FE program (using triangular plate elements) to compute the in-plane deformations of a cantilever thin plate with a central hole subject to in-plane stationary (non-rotating) radial forces due to contact between a roller bearing rollers and the ring. The bearing outer ring was modeled as an integral part of the plate (casing) and the authors recommended considering effect of the external forces rotation on the elastic housing deformations. Also, plate finite-elements were used, using existing FE programs, to model machine casings, see, for example, Choy, Ruan, Tu, Zakrajsek, Townsend (1992) where the supporting bearing linear springs and dampers were connected to the housing wall at fixed locations. In these papers (except the experimental part in [Taha and Crookail (1977)], the analyses are purely analytical. Such mathematical models are useful, in the disgn stage, where access to experimental work is costly/impossible, to provide the designer with, at least, guide lines.

In mechanical systems incorporating radial ball bearings, the ball force due to contact with the bearing rings is indeed a rotating load vector rolling over support, see, for example, Sankaravelu, Noah, and Burger (1994) and El-Saeidy (1998) where the housing with the outer ring fitted in it was treated rigid (except the Hertizian local elastic contacts). For elastic housings, effect of rotation of the ball force on the casing annulus (hole) surface dynamic deformations under the moving ball which in turn affect bearing tolearances and magnitude of the generated (reaction) forces should be considered. The contribution of the current paper is to present a FE based analysis procedure for the dynamic simulation of a machinery 2D elastic casing with a central hole subject to an in-plane rotating (moving) deflection dependent load. Although applications

---

[1] Damro-Salman, Desouk, Kafr-El-Sheikh, Egypt

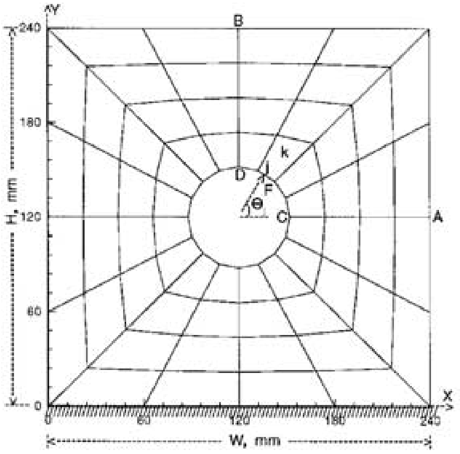

Figure 1 : FE discretization of the cantilevered plate

to rotating machinery incorporating radial ball bearings supported on elastic housings have been a guiding consideration, the analysis may have other similar applications.

2 Analytical Model

Figure 1 shows the FE discretization of a cantilevered plate rigidly fixed along the X axis with a central hole subject to an in-plane rotating deflection dependent load vector F. Here, the internal nodes (number 2, 4, 6, and 8, see Fig. 2) of each plate element are not shown. XYZ is a global coordinate system where the Z axis (not shown) points out of the paper. In Fig. 2, which describes the details of a typical plate finite-element under the action of the external moving (rotating) load vector F, the axes $\overline{XY}$ are fixed in space and parallel to the XY axes with the origin at the geometrical center of the housing annulus in the undeformed state. In Fig. 2, F is shown within the spatial domain of the kth finite-element. The radial position of the load vector measured from the horizontal direction (point O_j on the $\overline{X}$ axis) is given by $\theta_j = \Omega_c t$ (rad). Where Ω_c is the angular speed (rad/s) of the rotating load vector and t is the global time in seconds measured from the point O_j on the global boundary (the annulus cirumference). The plate element has 8 nodes with 2 degrees of freedom (DOF) each. Recall that the desired accuracy of the solution and idealization of the curved boundary (the hole surface in our case) can be achieved by using fewer number of 8-node isoparametric elements compared to an increased number of 6-node triangular elements with curved sides or vice versa. This is provided the number of DOF per node in each choice is the same. Thus, the selection of the 8-node C^o element is justified.

Let d_k^e and h_k^e denote, respectively, the global vector of the undeformed state position and the global vector of the elastic deformation of a generic point within the spatial domain of the kth element, such that

$$d_k^e = \begin{bmatrix} x & y \end{bmatrix}^T, \ h_k^e = \begin{bmatrix} u & v \end{bmatrix}^T \tag{1}$$

where the superscript e denotes the element and the subscript k stands for its number. x and y are the global positions along the X and Y, respectively. u and v are the global elastic displacements along the X and Y, respectively. Let z_k^e stands for the element 16×1 nodal point global coordinate vector and q_k^e refers to the kth element global displacement field vector, such that

$$z_k^e = \begin{bmatrix} x_j & y_j \end{bmatrix}^T, q_k^e = \begin{bmatrix} u_j & v_j \end{bmatrix}^T, j = 1,2,..,8 \tag{2}$$

The element global coordinate vector, d_k^e, and the elastic deformation vector, h_k^e, are related, respectively, to the vector of the element nodal points coordinates and the vector of the element nodal points variables, such that

$$d_k^e = Nz_k^e, h_k^e = Nq_k^e, N = \begin{bmatrix} N_j & 0 \\ 0 & N_j \end{bmatrix}, j = 1,2,..,8 \tag{3}$$

N is the 2×16 overall matrix of the element C^o shape functions whose enteries are

$$\begin{bmatrix} N_1 \\ N_2 \\ N_3 \\ N_4 \\ N_5 \\ N_6 \\ N_7 \\ N_8 \end{bmatrix} = \begin{bmatrix} \frac{-1}{4}(1-r)(1-s)(1+r+s) \\ \frac{1}{2}(1-r^2)(1-s) \\ \frac{-1}{4}(1+r)(1-s)(1-r+s) \\ \frac{1}{2}(1+r)(1-s^2) \\ \frac{-1}{4}(1+r)(1+s)(1-r-s) \\ \frac{1}{2}(1-r^2)(1+s) \\ \frac{-1}{4}(1-r)(1+s)(1+r-s) \\ \frac{1}{2}(1-r)(1-s^2) \end{bmatrix} \tag{4}$$

r and s are the element serendipity coordinates. Expressed in the XYZ system, the plate element kinetic and potential energies are $\frac{1}{2}(\dot{q}_k^e)^T M_k^e \dot{q}_k^e$ and $\frac{1}{2}(q_k^e)^T K_k^e q_k^e$, respectively where the element stiffness and consistent mass matrices K_k^e and M_k^e are

$$\begin{bmatrix} K_k^e \\ M_k^e \end{bmatrix} = \int_{-1}^{1}\int_{-1}^{1} \begin{bmatrix} t_k^e(B_k^e)^T D_k^e B_k^e \\ t_k^e \rho_k^e (N)^T N \end{bmatrix} det(J_k^e) dr ds \tag{5}$$

ρ_k^e, t_k^e, D_k^e, and B_k^e are the material mass density, the plate thickness, the matrix of the linearly elastic isotropic material constants for plane stress, and the global strain displacement matrix, respectively. $det(J_k^e)$ is the determinant of the element 2×2 jacobian matrix, J_k^e.

2.1 Plate Finite Element Load Vector due to In-Plane Deflection Dependent Moving Load

Some of the mathematical background in this section have been presented previously by El-Saeidy (1999) and since that work is still under publication consideration, the pertaining analyses presented there will be recalled concisely in the current article for the sake of completeness. Figure 2 depicts

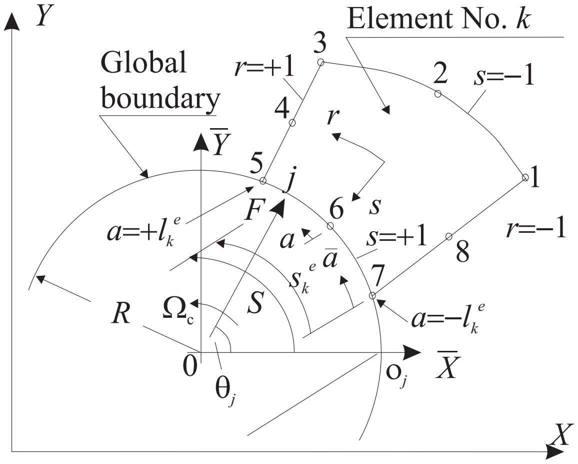

Figure 2 : A global boundary plate finite-element subject to an in-plane moving (rotating) load

a typical plate finite-element (number k) sharing the global boundary (the hole circumference) under the action of an inplane moving load vector. Where $\overline{a}$ is an element physical coordinate with its origin at node number 7 and is measured along the global boundary. Also, let us introduce another physical coordinate, a, that runs along the annulus circumference with its origin at the element midspan point along the global boundary (node number 6). The element physical length along the global boundary is $2\ell_k^e$ such that $a = +\ell_k^e$ at node number 5 and $a = -\ell_k^e$ at node number 7.

The load vector F is taken to be composed of two contributions and its amplitude, $\overline{F}$, is given by

$$\overline{F} = F_o + F(t) \tag{6}$$

where $F_o = \overline{F}_o t_k^e$ ($\overline{F}_o$ is a force per unit plate thickness) is a constant force and $F(t)$ is the deflection (time) dependent component which we model as

$$F(t) = K(\mid \delta_r \mid)^{3/2} \tag{7}$$

Here, $|\,.\,|$ is the absolute value and δ_r is the relative approach in the radial direction at the instantenous position of the rotating load F, such that

$$\delta_r = u_d \cos\theta_j + v_d \sin\theta_j \tag{8}$$

u_d and v_d are the X and Y components, respectively, of the elastic deformation vector of the point under the moving load (see Eq. 22). Equation 7 is based on the Hertzian contact between the ball bearing rotating elements and rings in the case of tight (zero) clearance (for example see, the bearing model [El-Saeidy (1998)]), with no oscillations of the bearing innner ring. In practice a situation like this can arise when the bearing inner ring is lightly fitted on a rigid and well balanced (i.e., no mass imbalance excitation) rotating shaft such that the journal lateral motions (if exist) are of negligible amplitudes. K (N/mm$^{3/2}$) is a constant which can be computed using the ball bearing analysis [Harris (1984)]. Furthermore, in a ball bearing assembly, the component F_o can arise from a preload or an interference fit in the housing, which in turn creates tight clearance. However, any other model(s) at the reader's disposal can be used. The reason for subjecting the elastic casing to only one moving force is to isolate the nonlinear interaction between the force and the elastic member from effects of other similar rotating forces. The extension of the analyses to the case of a train of moving loads is straightforward. The global dynamic load vector, F, has two components along the X and Y axes, F_x and F_y, respectively.

$$F = \begin{bmatrix} F_x & F_y \end{bmatrix}^T = \overline{F} \begin{bmatrix} \cos\Omega t & \sin\Omega t \end{bmatrix}^T \tag{9}$$

The instantenous global position of the moving load along the global boundary is determined by the global distance $S = Vt$, measured from the instant F starts rotation at the point O_j. $V = \Omega_c R$ is the circumferential speed of the moving load where R is the radius of the annulus and t is the global time coordinate with its origin at O_j. While the vector F is within the kth element global boundary, its position relative to node number 7 is measured by the local distance $s_k^e = V\bar{t}$ where $\bar{t}$ is a local (an element) time coordinate measured from the instant the moving load reaches node number 7. This local measure and the global measure S are related, such that $s_k^e = S - 2(k-1)\ell_k^e$ where k is the element number. It should be noted, however, that both S and s_k^e are measured along the same global boundary. Expressed in the XYZ frame, the element global external load vector due to the moving load vector is given by F_k^e, such that

$$F_k^e = \begin{cases} F\delta(\overline{a} - V\bar{t}) & \text{if } 2(k-1)\ell_k^e < S < 2k\ell_k^e \\ \underline{0}_2 & \text{otherwise} \end{cases} \tag{10}$$

Here, $\underline{0}_2$ is a 2 × 1 null vector. $\delta(\overline{a} - V\bar{t})$ is the dimensional Dirac delta function with both $\overline{a}$ and $V\bar{t}$ as defined earlier. Since the units of this delta function are those of $1/\overline{a}$, the vector F_k^e may be interpreted as a load per unit length (see Eq. 11). To rewrite $\delta(\overline{a} - V\bar{t})$ in terms of the coordinates r and s, let us introduce a new nondimensional coordinate, $\overline{g} = a/\ell_k^e$, (called hereafter the element global boundary natural coordinate). The coordinate $\overline{g}$ (not shown), whose origin is at node number 6, changes its value in a linear fashion from -1 at node number 7 to +1 at node number 5 along the global boundary.

From Fig. 2, the relation between the kth element two physical coordinates $\overline{a}$ and a is $\overline{a} = a + \ell_k^e$. Thus, $\delta(\overline{a} - V\bar{t}) = \delta(a + \ell_k^e - V\bar{t})$ which upon using the coordinate $\overline{g}$ and utilizing properties of the generalized delta function, we get $\delta(\overline{a} - V\bar{t}) = (1/\ell_k^e)\overline{\delta}(\overline{g} - (-1 + V\bar{t}/\ell_k^e))$. $\overline{\delta}(.)$ is the nondimensional delta function. The term $(-1 + V\bar{t}/\ell_k^e)$ assumes a value of -1 when the load arrives at node 7 and a value of +1 when the load departs at node number 5. Thus, this time dependent, and linearly varying, term measures the change in the coordinate $\overline{g}$ as the load progresses (rotates). Substitute $V\overline{t} = s_k^e$ into the right hand side of the last expression for $\delta(\overline{a}\text{-}V\overline{t})$ and then into Eq. 10, we get

$$F_k^e = \begin{cases} \frac{F}{\ell_k^e}\overline{\delta}(\overline{g} - \frac{s_k^e}{\ell_k^e} + 1) & \text{if } 2(k-1)\ell_k^e < S < 2k\ell_k^e \\ \underline{0}_2 & \text{otherwise} \end{cases} \tag{11}$$

Recall from Eq. 3 that $h_k^e = Nq_k^e$, the virtual change in the displacement field h_k^e, δh_k^e, is

$$\delta h_k^e = \begin{bmatrix} \delta u & \delta v \end{bmatrix}^T = N\delta q_k^e \tag{12}$$

δq_k^e is the virtual change in the vector field q_k^e. The virtual work of the vector F_k^e is given by δW_k^e.

$$\delta W_k^e = \int_{-\ell_k^e}^{\ell_k^e} (\delta h_k^e)^T F_k^e da \tag{13}$$

In this global boundary line integral, da (not shown) is the differential (infinitesimal) arc length on the global boundary. da may be computed using the global components of the infinitesimal chord length approxmating it, dx and dy, in the X and Y directions, respectively, and the Pathagorean theorem. To this end, $da = \sqrt{(dx)^2 + (dy)^2}$ where x and y are the global coordinates of a general point on the element global boundary. From Eqs. 1 and 2 into 3, then $\begin{bmatrix} x & y \end{bmatrix}^T = \mathrm{N}\begin{bmatrix} x_j & y_j \end{bmatrix}^T$. Recall that $N = N(r,s)$ and use the chain rule of differentiations, the total differentials dx and dy are

$$\begin{bmatrix} dx \\ dy \end{bmatrix} = \sum_{j=1}^{Nen} \begin{bmatrix} \frac{\partial N_j}{\partial r}x_j & \frac{\partial N_j}{\partial s}x_j \\ \frac{\partial N_j}{\partial r}y_j & \frac{\partial N_j}{\partial s}y_j \end{bmatrix} \begin{bmatrix} dr \\ ds \end{bmatrix} \tag{14}$$

Nen is the element number of nodes. Since on the global boundary s=+1 and r is a spatial variable, we have $ds = 0$. Use the da's expression and Eq. 14, then

$$da = R_k^e(r,1)dr \tag{15}$$

$$R_k^e(r,1) = \sqrt{(\textstyle\sum_{j=1}^{Nen} \frac{\partial N_j(r,1)}{\partial r}x_j)^2 + (\sum_{j=1}^{Nen} \frac{\partial N_j(r,1)}{\partial r}y_j)^2}$$

In Eq. 15, the partial derivatives of the element shape matrix enteries are computed along the global boundary where s=+1 and r changes its value in a linear fashion as explained above. The elements N_j in Eq. 4, show that only the components N_5, N_6, and N_7 will contribute to the right hand side of $R_k^e(r,1)$'s equation. And this not only saves CPU time but also serves as an essential pivot in deriving Eq. 21 as follows.

Use Eq. 12, $(\delta h_k^e)^T = (\delta q_k^e)^T(N)^T$. Recall that $N = N(r,s)$ should be replaced by $N(r,1)$ and substitute from Eq. 15 into Eq. 13 and since δq_k^e constitutes a set of only time dependent variables, we get

$$\delta W_k^e = (\delta q_k^e)^T \int_{-1}^{1} (N(r,1))^T F_k^e R_k^e(r,1)dr \tag{16}$$

Substitute from Eq. 11 into 16 and adjust the vector dimensions, then in a compact form, we have

$$\delta W_k^e = (\delta q_k^e)^T Q_k^e \tag{17}$$

Q_k^e is the element global generalized load vector associated with the global generalized deformation vector q_k^e, such that

$$Q_k^e = \begin{cases} \int_{-1}^{1} Z_1(r)dr & \text{if } 2(k-1)\ell_k^e < S < 2k\ell_k^e \\ \underline{0}_{16} & \text{otherwise} \end{cases} \tag{18}$$

$$Z_1(r) = R_k^e(r,1)(N(r,1))^T \frac{F}{\ell_k^e}\overline{\delta}(\overline{g} + 1 - \frac{s_k^e}{\ell_k^e})$$

where $\underline{0}_{16}$ is a 16×1 null vector. The integral in Eq. 18 in its current form is not amenable to evaluation because the delta function is expressed in terms of the coordinate $\overline{g}$ while the integration is with respect to r. However, this hurdle can be removed as follows. As it has been pointed out previously, the element nodal points number 1, 2, 3, 4 and 8 are free from any direct influence of the external applied load vector and this makes the coordinate r only affects the external forces applied to the nodal points 5, 6, and 7. That is, the applied forces at the element global boundary nodes are not explicit functions of any external forces that may exist at any of the other 5 nodal points and effect of r on the element external forces is limited to the linear variation in its value between the nodes number 7 and 5 on the global boundary. The same effect of the linear variation in value, along the global boundary, is a requirement for the coordinate $\overline{g}$, as well, as can be viewed from the above presentation. In other words, both the r and $\overline{g}$ coordinates are equivalent in their effects on the computation of the element load vector. Therefore, in the above integral, $\overline{g}$ can be replaced by r and the reverse is not allowed. To this end, Eq. 18 can be rewritten as

$$Q_k^e = \begin{cases} \int_{-1}^{1} Z_2(r)dr & \text{if } 2(k-1)\ell_k^e < S < 2k\ell_k^e \\ \underline{0}_{16} & \text{otherwise} \end{cases} \tag{19}$$

where the time dependent function $Z_2(r)$ is the same as $Z_1(r)$ (Eq. 18) except that $\overline{g}$ is replaced by r. Now, utilizing the properties of the Dirac delta function, Eq. 19 becomes

$$Q_k^e = \begin{cases} H_k^e(s_k^e)\frac{F}{\ell_k^e} & \text{if } 2(k-1)\ell_k^e < S < 2k\ell_k^e \\ \underline{0}_{16} & \text{otherwise} \end{cases} \tag{20}$$

$$H_k^e(s_k^e) = R_k^e(\frac{s_k^e}{\ell_k^e} - 1, 1)(N(\frac{s_k^e}{\ell_k^e} - 1, 1))^T$$

Thus, the element global generalized load vector, Q_k^e, associated with the generalized vector q_k^e can be evaluated at any instantenous position along the element global boundary by evaluating the matrix function $H_k^e(s_k^e)$ at the corresponding instantenous and nondimensional position $(-1 + s_k^e/\ell_k^e)$. And then multiplying it by the global load vector F divided by the element half length along global boundary, ℓ_k^e. However, if the nodal point number 6 is located at the midspan point of the element global boundary, which is the assumption in our case, the function $R_k^e(-1+s_k^e/\ell_k^e,1)$ will always be equal to ℓ_k^e. To this end, Q_k^e is given by

$$Q_k^e = \begin{cases} (N(\frac{s_k^e}{\ell_k^e}-1,1))^T F & \text{if } 2(k-1)\ell_k^e < S < 2k\ell_k^e \\ \underline{0}_{16} & \text{otherwise} \end{cases} \tag{21}$$

However, in this case, Eq. 20 can be used to check success of the computer implementation of the formulation. That is, a successful digital implementation should always yield the instantenous value of the function $R_k^e(-1+s_k^e/\ell_k^e,1)$ equal to ℓ_k^e while the load vector is traveling along the global boundary of the kth element.

Let $\begin{bmatrix} u_d & v_d \end{bmatrix}^T$ denotes the global displacement vector of the point under the moving load. This deformation field vector can be obtained by specializing h_k^e of Eq. 3 to the rolling point on the element global boundary, such that

$$\begin{bmatrix} u_d \\ v_d \end{bmatrix} = N(-1+\frac{s_k^e}{\ell_k^e},1)q_k^e \tag{22}$$

where u_d and v_d are the global elastic motions along the X and Y axes, respectively. Similarily, if $\begin{bmatrix} x_d & y_d \end{bmatrix}^T$ denotes the global coordinate vector of the point under the moving load, then the vector d_k^e of Eq. 3 gives

$$\begin{bmatrix} x_d \\ y_d \end{bmatrix} = N(-1+\frac{s_k^e}{\ell_k^e},1)z_k^e \tag{23}$$

If the element nodal points and its serendepity coordinates, r and s, are arranged in such a manner that on the global boundary the coordinate r has a constant value and s changes its value in a linear fashion, the ensuing changes in the right hand side of Eq. 19 can easily be identified. Although presenting the final equations necessary for producing the reported results, namely, Eqs. 21 to 23 and Eqs. 1 to 9 may be sufficient for some readers. For others with interest in extending the work, for example, to a casing under a 3D load vector, etc, the analyses between Eqs. 9 and 21 may be of interest.

2.2 *Equations of Motion and Solution Scheme*

Use the element energy expressions and apply Lagrange's equations, the element equations of motion are $M_k^e\ddot{q}_k^e + K_k^e q_k^e = Q_k^e$. Let the system overall global mass and stiffness matrices be M, and K, respectively, and Q be the time dependent overall global load vector, each obtained by assembling the corresponding contribution from the indivudal elements using the one-dimensional (1D) array scheme for banded/sparse matrices [El-Saeidy (1993)]. Let q denotes the system overall global displacement field, the global system of equations of motion is $M\ddot{q}+Kq = Q$. Premultiplying by $(\Phi_N)^T$ and using the transformations $[q\ \dot{q}\ \ddot{q}]^T = \Phi_N[\eta\ \dot{\eta}\ \ddot{\eta}]^T$ where η is the modal displacement vector and Φ_N is the normalized (with respect to M) modal matrix obtained by solving the eigenvalue problem, we get $\ddot{\eta}+\underline{\omega}^2\eta = \overline{F}$. $\overline{F} = (\Phi_N)^T Q$ is the load vector expressed in the normal coordinates representation and $\underline{\omega}^2$ is the spectral matrix. The scheme used to solve this uncoupled system is presented in the Appendix. Using this scheme, the program 'DAMRO 1' has been used successfully in the analysis of rotating/nonrotating structures acted upon by moving loads. See, for example, [El-Saeidy (2000)] where the finite-element results are in exact agreement with the reported results which were obtained using exact solution and a Laplace transformation technique as well as the Runge-Kutta numerical integrator. In the current work, we used $\Delta t = 2\times10^{-6}$ s.

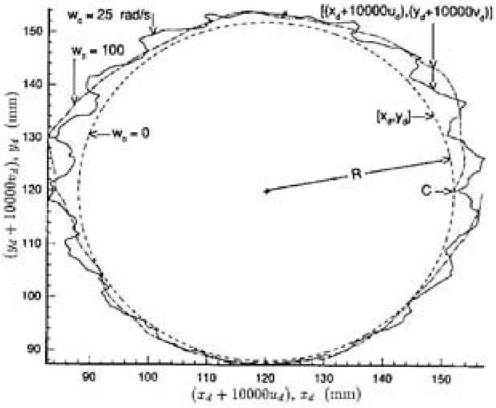

Figure 3 : Orbit $(x_d+\alpha u_d)$ vs $(y_d+\alpha v_d)$ for Ω_c = 0, 25, 100 rad/s, $\alpha = 10000$; x_d vs y_d, $\overline{F} = F_o = 500$ N, $N_{rv} = 1$ [El-Saeidy (1999)]

3 Results and Discussion

The input data are: F_o=500 N, $K = 10^7$ N/mm$^{3/2}$, H=W=240 mm, E^e=200 GPa, $\rho^e = 750$ kg/m^3, $\nu^e = 0.3$, Ω_c= 350 rad/s (f_c = 55.6818 Hz), N_{rv} = 300 = number of load revolutions (cycles). In the FE discretization (Fig. 1), the element midspan nodal points (number 2,4,6,8) are masked. The eigenvalue problem is solved using different number of elements and samples of the results are tabulated in Tab. 1 where $\overline{f}$ is the natural frequency with the subscript denotes its number and the superscripit denotes the number of elements used in each mesh. For accurate mapping of the casing curved global boundary (annulus surface), we used the 64 elements discretization. Table 2 tabulates the first sixteen natural tones used in the modal analysis.

Before we present results, we reproduce one plot from [El-Saeidy (1999)] showing the dynamic deformations of the housing annulus under a moving load with constant magnitude ($\overline{F} = F_o = 500\ N$) for w_c (Ω_c in the formulation) = 0, 25, 100 rad/s. Here, in Fig. 3, x_d and y_d are the X and Y global positions of the moving point around the circumference, computed

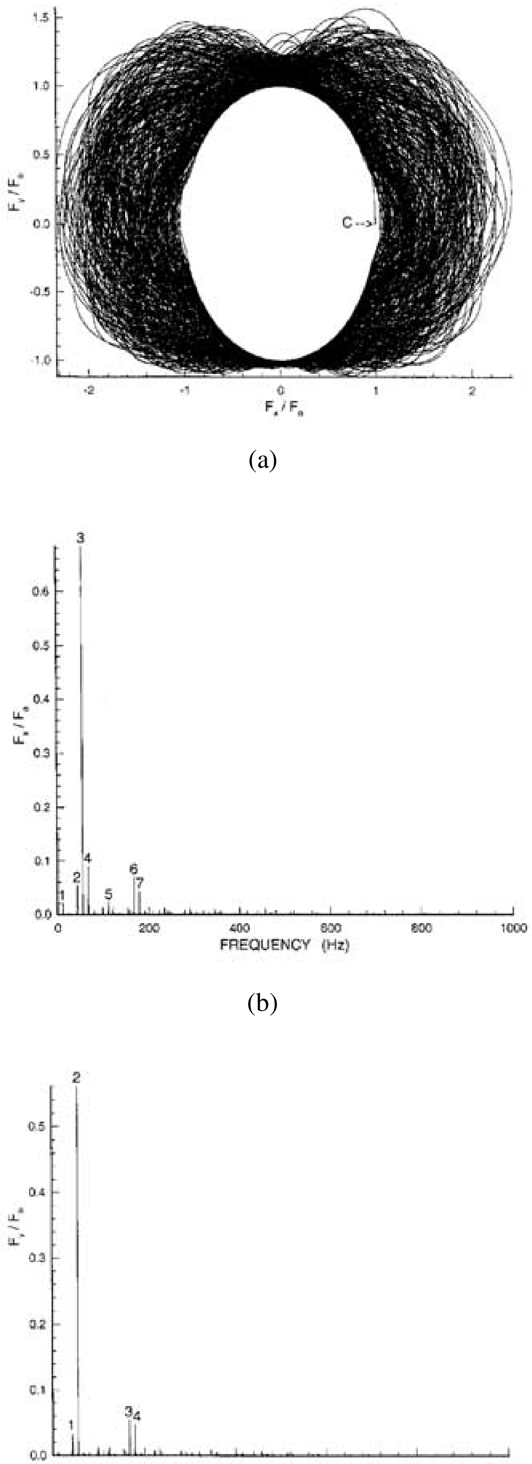

(a)

(b)

(c)

Figure 4 : (a) Nondimensional load orbit F_x/F_o vs F_y/F_o, F_o = 500 N, (b) FFT of F_x/F_o, (c) FFT of F_y/F_o

Table 1 : Samples of 3 meshes eigenvalues, Hz

$(\overline{f}_1^{32}, \overline{f}_1^{48}, \overline{f}_1^{64})$	=	(71.595, 71.525, 71.242)
$(\overline{f}_2^{32}, \overline{f}_2^{48}, \overline{f}_2^{64})$	=	(183.954, 183.803, 182.858)
$(\overline{f}_3^{32}, \overline{f}_3^{48}, \overline{f}_3^{64})$	=	(210.620,210.469, 210.097)
$(\overline{f}_{12}^{32}, \overline{f}_{12}^{48}, \overline{f}_{12}^{64})$	=	(603.498, 602.532, 601.397)

Table 2 : Natural frequencies used in analysis, Hz

$(\overline{f}_1, \overline{f}_2)$	=	(71.242, 182.858)
$(\overline{f}_3, \overline{f}_4)$	=	(210.097, 290.553)
$(\overline{f}_5, \overline{f}_6)$	=	(301.367, 361.885)
$(\overline{f}_7, \overline{f}_8)$	=	(451.762, 472.995)
$(\overline{f}_9, \overline{f}_{10})$	=	(555.931, 572.175)
$(\overline{f}_{11}, \overline{f}_{12})$	=	(594.796, 601.397)
$(\overline{f}_{13}, \overline{f}_{14})$	=	(670.564, 685.403)
$(\overline{f}_{15}, \overline{f}_{16})$	=	(751.222, 775.623)

using Eq. 23, and u_d and v_d are their counterparts global deformations, calculated using Eq. 22. The surface $[x_d, y_d]$, which corresponds to the global boundary configuration for $\Omega_c = 0$ (before the external excitation is applied) is a circle of radius R = 32 mm and this demonstrates success of the formulation computer implementation. Both u_d and v_d are multiplied by a factor $\alpha = 10^4$ and then superimposed on the corresponding instantenous positions x_d and y_d, respectively, and plotted as $(x_d + \alpha u_d)$ vs $(y_d + \alpha v_d)$. Recall that the load starts and terminates rotation at point C, we remark that the deformable surface, $[(x_d + \alpha u_d), (y_d + \alpha v_d)]$, does not close onto itself with the minimum deviation at the closing point (point C) corresponds to the plot for Ω_c = 25 rad/s. As the speed of rotation increases, the deformation amplitude decreases and the surface becomes more smoother. This is because at lower speeds, the elastic motions have enough time to build up. The deformation amplitudes are always positive (contraction) with the region of the highest overall amplitudes stacked in the neighberhoods of $\theta_j = 0, 180^o$. The elliptical shape and the deformation pattern of the annulus surface (see plot for Ω_c = 25 rad/s) qualitatively resemble the experimental/FE results of Taha and Crookail (1977). Recall that the results of Taha and Crookail are for a plate which is made from epoxy resin material (to allow convenient deformations to be obtained with quite small loads) and the casing was loaded by a radial force acting on a nonrotating rigid shaft which in turn is supported on the bearing rollers.

Now, we present results of the digital simulation for $N_{rv} = 300$.

Figure 4a, shows the generated components of the dynamic load vector in a nondimensional polar format where we see that the load trajectory does not close onto itself (observe the start point C). The orbit indicates that the force F_x is of overall higher amplitudes compared to the component F_y. This is because the housing is more flexible in the horizontal direction compared to the vertical direction due to the rigid support being along the X axis (see also Fig. 5a, to be discussed soon where we observe there that the elastic deformations of the annulus surface are of minimum amplitudes when the rotating load vector is in the vicinity of the vertical axis) in addition to the fact that at the start of the load rotation F_x is of maximum amplitude whereas the force F_y which starts with zero amplitude requires more time to reach its first peak. And this agrees with the physical intution. For brevity, we did not include the time domains for F_x and F_y, however, their spectra are shown in Figs. 4b and 4c, respectively. Prior to the FFT computations, the time record is zero meaned and windowed using Hanning's window. The spectrum for F_x is of higher overall energy content compared to its counterpart for F_y. In the X direction, the dominant tone f_3 = 55.6707 Hz is contributed by the forcing frequency, f_c, and in the Y direction f_2 is due to f_c as well. In Fig. 4b, the other marked vibrations are (f_1, f_2, f_4, f_5, f_6, f_7) = (12.786, 43.392, 67.949, 111.461, 167.129, 179.407) Hz and their sources are (Δf, f_c - Δf, $f_c + \Delta f$, $2f_c$, $3f_c$, $\overline{f}_6$ - $\overline{f}_2$) where $\Delta f = 4f_c$ - $\overline{f}_3$ = 12.630 Hz. As we see these tones show modulation of the external excitation frequency through the natural tones or vice versa. In the Y direction, the other marked peaks are (f_1, f_3, f_4) = (f_c - Δf, $3f_c$, $\overline{f}_6$ - $\overline{f}_2$).

Figure 5a depicts the global deformations of the housing hole, in a polar format under the moving load. The time domain of the compound wave $(x_d + \alpha u_d)$ and the pure deformation wave u_d are shown in Figs. 5b and 5c, respectively, and for brevity the domains for the corresponding waves in the Y direction are not presented. As we see from the state plane and Figs. 5b and 5c, u_d has a maximum amplitude of about 1.8 μm compared to a maximum amplitude of about 0.72 μm for v_d. The largest amplitudes of the elastic deformation are staked in the horizontal direction region and the smallest ones are confined to the zone in the vicinity of the vertical axis. These patterns in the annulus circumferential dynamic deformations contribute to the trends in the generated dynamic fores as we have just seen in Fig. 4a. Practically, this means that the regular variations in these deformations and hence the ensuing variations in the generated nonlinear forces can create/accelerate fatigue in the elastic components of the assembly.

When the time domain in Fig. 5b and its counterpart in the Y direction (not shown) are sampled once per forcing frequency period and projected onto the plane (x_d+αu_d, y_d+αv_d), the resulting Poincare' first return maps obtained using the variables (x_d+αu_d) and (y_d+αv_d) are given in Figs. 5d. and 5e, respectively. In both directions, the map occupies an elliptical area with the ellipse major axes runs along the identity map (45 deg

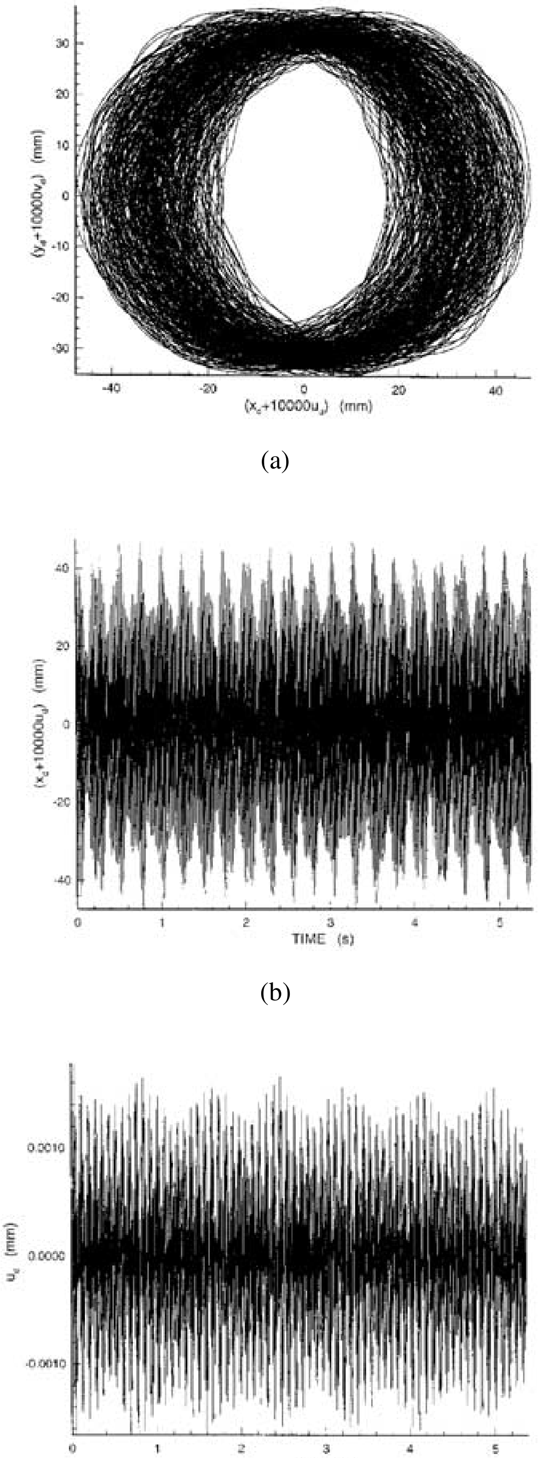

(a)

(b)

(c)

Figure 5 : (a) Orbit (x_d + αu_d) vs (y_d + αv_d), (b) (x_d + αu_d) vs time, (c) u_d vs time, (d) map $(x_d + \alpha u_d)_n$ vs $(x_d + \alpha u_d)_{n+1}$, (e) map $(y_d + \alpha v_d)_n$ vs $(y_d + \alpha v_d)_{n+1}$, (f) FFT of u_d, (g) FFT of v_d, α = 10000

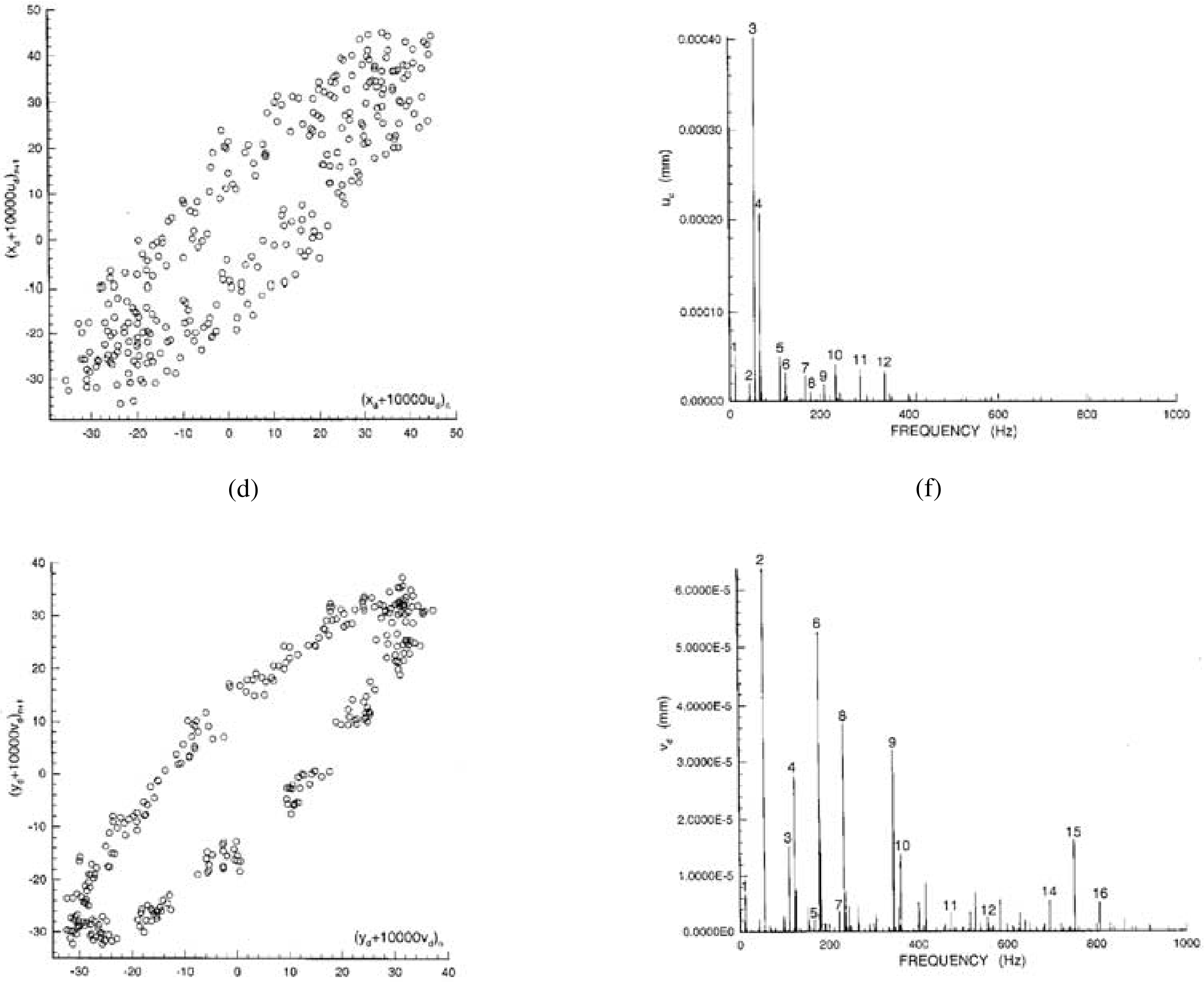

(d) (f)

(e) (g)

Figure 5 : (continued)

line). Each of the two maps is not one to one (i,e., the variable amplitude at the end of the current cycle can not be obtained from the variable amplitude at the end of the previous cycle). This may be an indication of a higher dimensional dynamical system. The points of the X direction map tend to fill up the area of the ellipse uniformly compared to an island-like pattern in the Y direction map. We may observe that the system's dynamical behavior in one of the two orthogonal directions can not be inferred completely from the system's behavior in the other direction. Moreover, we recall that [Ehrich (1991)] reported a beating signal (forced vibration) and its Poincare' return map which occupies an elongated ellipse with its major axis on the 45 deg line.

The spectra of the elastic deformations u_d and v_d are illustrated in Figs. 5f and 5g, respectively. In each of the two plots, the largest vibration is attributed to f_c. In Fig. 5f, the other marked peaks f_1, f_2, f_4 to f_{12}, respectively, are contributed by Δf, f_c-Δf, f_c+Δf, $2f_c$, $2f_c$+Δf, $3f_c$, $\overline{f}_6$-$\overline{f}_2$, $\overline{f}_3$, $4f_c + \Delta f$, $\overline{f}_4$, and $6f_c + \Delta f$, respectively. In Fig. 5g, the vibrations f_1, f_2, f_3, f_4, f_5, f_6, f_8, and f_9 coincide with the tones f_1, f_3, f_5, f_6, f_7, f_8, f_{10}, and f_{12}, respectively, of Fig. 5f. Moreover, in Fig. 5g, f_7, f_{10}, f_{11}, f_{12}, f_{14}, f_{15}, f_{16} are attributed to $4f_c$, $\overline{f}_6$, $\overline{f}_8$, $\overline{f}_{10}$, $\overline{f}_{15}$-f_c, $\overline{f}_{15}$, and $\overline{f}_{15}$+f_c, respectively. As we see the participation of the system's natural frequencies is obvious. It is interesting to note that in the FFT for the velocity $\dot{u}_d$ (not shown) the dominant vibration is at f_c and in the FFT for $\dot{v}_d$ (also not shown) the largest tone is at $\overline{f}_{15}$.

Before we conclude the paper, we present the spectrum for the horizontal velocity $\dot{U}_A$ measured at point A on the casing outer surface (Fig. 1) in Fig. 6a and the FFT for the vertical

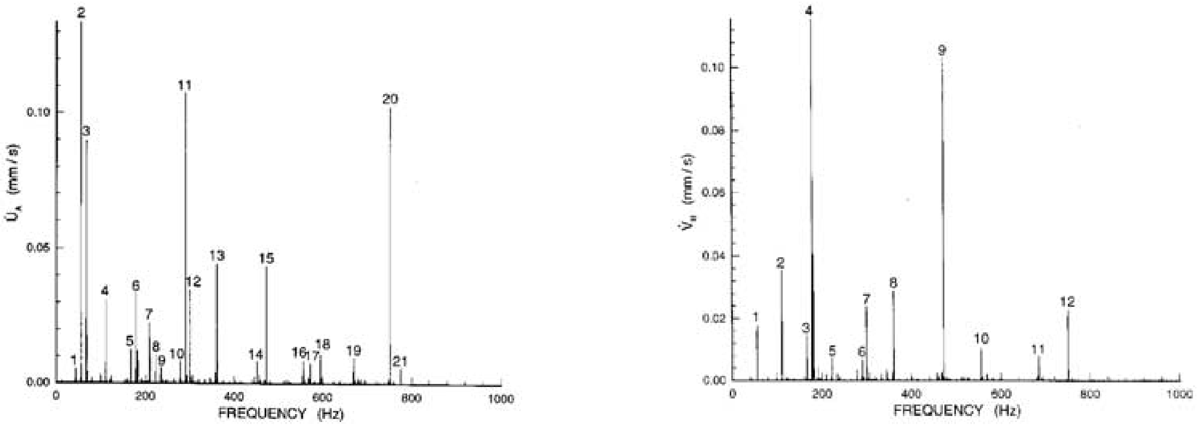

(a) (b)

Figure 6 : (a) FFT of the casing velocity at point A, $\dot{U}_A$, (b) FFT of the casing velocity at point B, $\dot{V}_B$

velocity $\dot{V}_B$ measured at point B in Fig. 6b (no time domains are included). In the horizontal directions, the marked tones f_1 to f_{21} are contributed by f_c - Δf, f_c, $f_c + \Delta f$, $2f_c$, $3f_c$, $\overline{f}_6$-$\overline{f}_2$, $\overline{f}_2$, $4f_c$, $4f_c + \Delta f$, $5f_c$, $\overline{f}_4$, $\overline{f}_5$, $\overline{f}_6$, $\overline{f}_7$, $\overline{f}_8$, $\overline{f}_9$, $\overline{f}_{10}$, $\overline{f}_{11}$, $\overline{f}_{14}$, $\overline{f}_{15}$, $\overline{f}_{16}$. In the vertical direction, however, the vibrations f_1 to f_{10} and f_{12}, respectively, correspond to the spikes f_2, f_3, f_5, f_6, f_8, f_{11}, f_{12}, f_{13}, f_{15}, f_{16}, and f_{20}, respectively, in Fig. 6a. As we see, the system's natural frequencies appear markedly in the spectrum measured at the casing outer surface. Moreover, the largest vibration in the X direction, f_2, and the largest tone in the Y direction, f_4, do not coincide. And this recommends using one vibration measuring probe in each of the two orthogonal directions, respectively, to avoid missing catastrophic failure enducing vibrations.

4 Conclusions

A procedure, using an isoparametric FE formulation, is presented for the vibration analysis of machinery 2D elastic casing with central hole subject to an in-plane moving (rotating) deflection dependent load. The Hertizian contact theory pertaining to contact between the ball bearing balls and rings is used to model the nonlinear elastic coupling between the external moving load and the housing vibrations. The equations of motions are obtained using Lagrange's equations and decoupled using the normal coordinates representation and then solved using a special numerical integration scheme. The analyses are implemented in the FE program 'DAMRO 1' and used to study elastic deformations of the annulus surface under the moving load. The results are discussed using time domain, motions in the state plane, Poincare' return map, and FFT. The results in time domain show that the overall amplitudes of the deformation vector around the casing hole circumference and hence amplitudes of the dynamic load vary between maximum along the X direction (direction of the casing rigid support, Fig. 1) and minimum in the orthogonal direction. These cyclic variations can initiate/accelerate fatigue in the elastic components of the system. The spectra of the velocities measured at the outer surface of the housing ($\dot{U}_A$, $\dot{V}_B$) are dominated by the system's natural frequencies. Moreover, the spectra of these velocities recommend us to use one vibration measuring probe in the horizontal direction and another probe in the vertical direction, to capture all the important vibrations. The application of the presented analyses to a complete dynamical system such as, for example, a ball bearing elastic support configuration is straightforward.

References

Adams, M. L. (1980): Nonlinear dynamics of flexible multi-bearing rotors. *Journal of Sound and Vibration*, vol. 71, no. 1, pp. 129–144.

Choy, F. K.; Ruan, Y. F.; Tu, Y. K.; Zakrajsek, J. J.; Townsend, D. P. (1992): Modal analysis of multiple gear systems coupled with gearbox vibrations. *ASME Journal of Mechanical Design*, vol. 114, pp. 486–497.

Ehrich, F. F. (1991): Some observations of chaotic vibration phenomena in high speed rotordynamics. *Journal of Vibration and Acoustics*, vol. 113, pp. 50–57.

El-Saeidy, F. M. A. (1993): *DAMRO 1: A General Purpose Finite Element Program.*

El-Saeidy, F. M. A. (1998): Finite element modeling of rotor-shaft-rolling bearing systems with consideration of bearing nonlinearities. *Journal of Vibration and Control*, vol. 4, no. 5, pp. 541–602.

El-Saeidy, F. M. A. (1999): Finite element vibration analysis of a cantilever plate with central circular hole subject to an inplane moving (rotating) load. *The Journal of The Acoustical society of America, accepted for publication*.

El-Saeidy, F. M. A. (2000): Finite element dynamic analysis of a rotating shaft with or without nonlinear boundary conditions subject to a moving load. *Nonlinear Dynamics*, vol. 21, no. 4, pp. 377–408.

Fryba, L. (1972): *Vibration of Solids and Structures Under Moving Load*. Noordhoff, Leiden.

Harris, T. A. (1984): *Rolling Bearing Analysis*. John Wiley, New York.

Laura, P. A.; Gutherrez, R. H. (1998): Transverse vibrations of a thin rectangular plate subjected to a non-uniform stress distribution field. *Journal of Sound and Vibration*, vol. 210, no. 4, pp. 559–565.

Leissa, A. W.; Ayoup, E. F. (1988): Vibration and buckling of a simply supported rectangular plate subjected to a pair of in-plane concentrated forces. *Journal of Sound and Vibration*, vol. 127, no. 1, pp. 155–171.

Sankaravelu, A.; Noah, S. T.; Burger, C. P. (1994): Bifurcation and chaos in ball bearings. In *ASME Winter Annual Meeting, Symposium on Stochastic and Nonlinear Dynamics*, pp. 313–325, AMD-vol. 192, DE-vol. 78, Chicago.

Taha, M. M. A.; Crookail, J. R. (1977): Rolling bearings for machine tools-comparative evaluation by a new experimental technique and by finite element analysis. *Inernational Journal of Machine Tools Design and Research*, vol. 17, pp. 179–190.

Taheri, M. R.; Ting, E. C. (1988): Dynamic response of plate to moving loads: finite element method. *Computers & Structures*, vol. 34, pp. 509–521.

Yang, T. Y. (1986): *Finite Element Structural Analysis*. Prentice-Hall, NJ.

Appendix A: The numerical integration scheme

$$\begin{aligned}
\eta_s(t_j+\Delta t) &= \left[\eta_s(t_j) - \frac{\overline{F}_s(t_j)}{(\omega_s)^2}\right]\cos(\omega_s\Delta t) \\
&\quad + \frac{\dot{\eta}_s(t_j)}{\omega_s}\sin(\omega_s\Delta t) + \frac{\overline{F}_s(t_j)}{(\omega_s)^2}, \\
\dot{\eta}_s(t_j+\Delta t) &= \left[\frac{\overline{F}_s(t_j)}{\omega_s} - \omega_s\eta_s(t_j)\right]\sin(\omega_s\Delta t) \\
&\quad + \dot{\eta}_s(t_j)\cos(\omega_s\Delta t), \\
\ddot{\eta}_s(t_j+\Delta t) &= \overline{F}_s(t_j) - (\omega_s)^2\eta_s(t_j+\Delta t), \\
&\quad s = 1,2,3,..,Nf. \qquad (24)
\end{aligned}$$

ω_s and Nf are the circular natural frequency and the number of retained modes, respectively. The η_s and $\dot{\eta}_s$ expressions have been presented in [Adams (1980)] without derivation. In their derivation [El-Saeidy (1998)], the force $\overline{F}_s(t_j)$ is assumed to be constant during time interval $t_j \leq t \leq t_{j+1}$ (i.e. time step has to be small).